Opto-Electronic Advances

Review

2018, Vol. 1, No. 3

DOI: 10.29026/oea.2018.180004

Germanium-tin alloys: applications for optoelectronics in mid-infrared spectra

Cizhe Fang[1], Yan Liu[1], Qingfang Zhang[2], Genquan Han[1]*, Xi Gao[1], Yao Shao[3], Jincheng Zhang[1] and Yue Hao[1]

We summarize our work of the optoelectronic devices based on Germanium-tin (GeSn) alloys assisted with the Si_3N_4 liner stressor in mid-infrared (MIR) domains. The device characteristics are thoroughly analyzed by the strain distribution, band structure, and absorption characteristics. Numerical and analytical methods show that with optimal structural parameters, the device performance can be further improved and the wavelength application range can be extended to 2~5 μm in the mid-infrared spectra. It is demonstrated that this proposed strategy provides an effective technique for the strained-GeSn devices in future optical designs, which will be competitive for the optoelectronics applications in mid-infrared wavelength.

Keywords: optoelectronics; germanium-tin alloys; mid-infrared spectra

Fang C Z, Liu Y, Zhang Q F, Han G Q, Gao X *et al*. Germanium-tin alloys: applications for optoelectronics in mid-infrared spectra. *Opto-Electronic Advances* **1**, 180004 (2018).

Introduction

It is known to all that Group IV semiconductors have been widely applied in electronic devices due to their compatibility with mature complementary metal-oxide-semiconductor (CMOS) technologies and excellent electronic transport properties. However, low luminous efficiency caused by their indirect-bandgap limits their applications in photonic functional devices. Recently, a new technology based on incorporating Sn into Ge has triggered a tremendous interest for the accessibility of the direct bandgap material[1-6]. The pioneering work has been made by R. Soref and C. H. Perry in ref. [7]. After that, subsequent theoretical studies[8-11] revealed that an indirect-bandgap material can be tuned to be a direct-bandgap one by increasing the substitutional Sn concentration in the Ge lattice. Moreover, the incorporation of Sn in the Ge lattice not only yields significant red shifts in the band gap energies but also makes it a possible candidate as the gain medium[12,13], which indicates the potential applications of photonics in the mid-infrared (MIR) regions[14-17]. Up to now, different kinds of efficient devices based on GeSn have been fabricated[13,18], including photodetectors and lasers with a response up to 2 μm.

However, there is a trade-off between high Sn composition and direct bandgap in GeSn based devices due to the fact that solid solubility resulting from high Sn composition would be destructive to the overall function of the optoelectronic device[19]. Furthermore, the thermal stability of GeSn film caused by high Sn content becomes an obstacle to device fabrication[20-24]. By inducing a tensile strain into GeSn alloys, the Sn composition can be reduced to achieve direct bandgap compared with the relaxed one[2,25,26], benefiting their light emission efficiency[27,28]. Therefore, silicon nitride (SiN_x) films are used as an external stressor to induce tensile or compressive strain into semiconductor[29-32], which poses a strategy to improve the optical performance of the strained GeSn-based structures.

We sum up the work of different kinds of optoelectronic devices based on GeSn alloys with the assistance of the Si_3N_4 liner stressor. Analytical calculations show that the tensile strain induced by Si_3N_4 liner in GeSn contributes to both device performance and the extension of

[1]Wide Bandgap Semiconductor Technology Disciplines State Key Laboratory, School of Microelectronics, Xidian University, Xi'an 710071, China; [2]Key Laboratory for Informatization Electrical Appliances of Henan Province, School of Electric and Information Engineering, Zhengzhou University of Light Industry, Zhengzhou 450002, China; [3]State Key Laboratory of Power Grid Security and Energy Conservation, China Electric Power Research Institute, Beijing 100192, China

* Correspondence: G Q Han, E-mail: hangenquan@ieee.org

Received 6 March 2018; accepted 10 April 2018; accepted article preview online 12 April 2018

optical absorption spectrum. It is demonstrated that the proposed strategy could expand the application spectrum of group IV based devices, which will find important applications in the novel optoelectronic applications.

Device design and characteristic

Photodetector

It is worth noting that employing the tensile strained GeSn alloys achieves a material with improved absorption coefficient α in MIR ranging, which provides an effective technique for extending the absorption edge of GeSn to mid-infrared wavelength. Here, we discuss three photodetectors based on different strained GeSn architectures. Figure 1(a) shows a conceptual illustration of the GeSn on Si on oxide undercladding pedestal (SOUP) waveguide. The 3-D schematics of GeSn pillar and fin array detectors are shown in Fig. 1(b) and 1(c), respectively. The tensile strain is introduced in the GeSn material by the Si_3N_4 liner stressor.

To better analyze the influence of the strain on the energy band, the *E-k* energy band diagrams of the relaxed and tensile strained $Ge_{0.90}Sn_{0.10}$ in three different detectors are plotted and compared in Fig. 2. It is observed that in contrast to relaxed GeSn, the $E_{G,\Gamma}$ is obviously reduced in tensile strained GeSn because there is a decline in the energy of Γ conduction valleys. It is clear that the $E_{G,\Gamma}$ of tensile strained GeSn in pillar detector exhibits a larger attenuation than that of fin detector. The impacts of geometric parameters on the energy band structure in fin and pillar detectors are discussed in detail in ref. [33]. What's more, the impact of Sn content on the *E-k* energy band for relaxed and tensile strained GeSn is analyzed in ref. [26]. It is concluded that by utilizing the Si_3N_4 liner stressor, the $E_{G,\Gamma}$ of GeSn alloy can be reduced, which is potential to extend the cutoff wavelength of various photonic devices into the MIR region.

In order to evaluate the performance of the proposed photodetectors, we calculate the absorption coefficient α, a key parameter for determining the detection spectrum of the detector, by equation (1) [34]:

$$\alpha(\hbar\omega)=\frac{\alpha_b}{(2\pi)^2}\frac{2\mu^{\frac{3}{2}}}{\hbar^2}(\hbar\omega-E_{G,\Gamma})^{\frac{1}{2}} \quad , \qquad (1)$$

where $\hbar$ is the reduced Plank constant $h/2\pi$, ω is the angular frequency, and μ is the reduced mass, which can be calculated by $m_e^* m_h^* / (m_e^* + m_h^*)$. The electron and

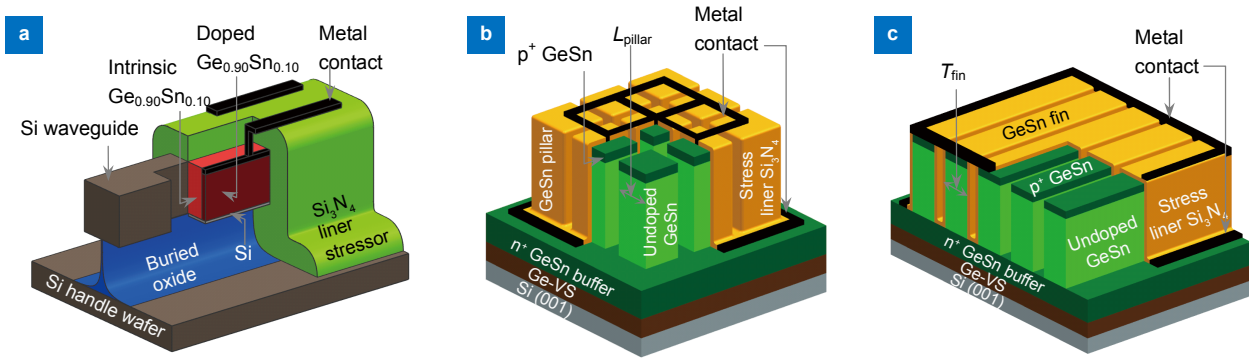

Fig. 1 | 3D schematics of the designed GeSn photodetectors based on different architectures. (**a**) GeSn on SOUP waveguide integrated with the Si_3N_4 liner stressor. Three-dimensional schematics of GeSn detectors with (**b**) pillar and (**c**) fin array integrated with the Si_3N_4 liner stressor on Si platform. Figure reproduced from: (**a**) ref. [26], Optical Society of America; (**b**, **c**) ref. [33], IEEE.

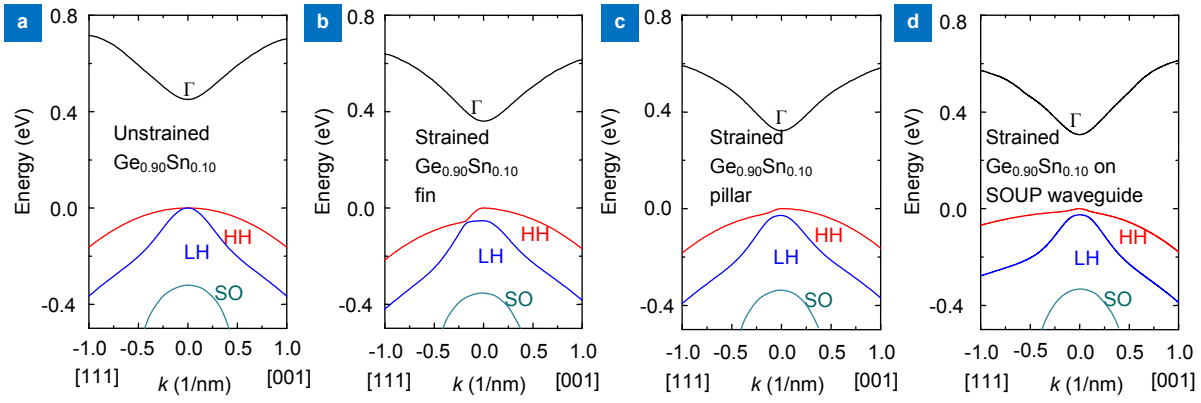

Fig. 2 | *E-k* energy band diagrams of relaxed and strained GeSn devices. (**a**) Relaxed $Ge_{0.90}Sn_{0.10}$. (**b**) Tensile strained $Ge_{0.90}Sn_{0.10}$ in fin array detector with the L_{pillar} of 200 nm. (**c**) Tensile strained $Ge_{0.90}Sn_{0.10}$ in pillar array detector with the L_{pillar} of 200 nm. (**d**) Tensile strained $Ge_{0.90}Sn_{0.10}$ on SOUP waveguide. Figure reproduced from: (**a**, **b**, **c**) ref. [33], IEEE; (**d**) ref. [26], Optical Society of America.

hole effective masses (m_e^* and m_h^*) are extracted from *E-k* energy band diagrams based on

$$m^* = (\frac{1}{\hbar^2} \cdot \frac{\mathrm{d}^2 E}{\mathrm{d}k^2})^{-1} \quad .$$

The α_b is given by

$$\alpha_b = \frac{2\pi e^2 E_{G,\Gamma}(E_{G,\Gamma} + \Delta)}{3n\varepsilon_0 \omega c m_e (E_{G,\Gamma} + \frac{2\Delta}{3})} \quad . \qquad (2)$$

In equation (2), n is the refractive index, ε_0 is the vacuum permittivity, c is the velocity of light, m_e is the electron mass, and Δ is the spin-orbit splitting.

Figure 3(a) shows that the calculated absorption coefficient α is modeled as a function of optical wavelength for relaxed and strained $Ge_{0.90}Sn_{0.10}$ in fin and pillar array detectors with different geometric parameters. It can be clearly seen that the optical response spectra of both strained $Ge_{0.90}Sn_{0.10}$ fin and pillar detectors are wider than that of relaxed detector. Besides, the pillar detector exhibits a larger cutoff frequency than fin detector when L_{pillar} and T_{fin} are equal. With the decrease in fin and pillar dimensions, the cut-off wavelengths display an obvious redshift. It should also be noted that the cut-off wavelengths are extended to be 4.35 μm with the L_{pillar} of 100 nm. As shown in Fig. 3(b), we investigate the impact of the Sn content on the cut-off wavelengths of both the relaxed and strained devices. A significant redshift of absorption edge can be obtained in the strained devices. Furthermore, the cut-off wavelength performs a greater improvement with a larger Sn composition. All the enhancements in the cut-off wavelength can be speculated that there is an attenuation in the $E_{G,\Gamma}$ of GeSn.

Optical modulators

In this section, we theoretically investigate tensile strained GeSn electro-absorption modulator based on the Franz-Keldysh (FK) effect. As depicted in Fig. 4, α is modeled as a function of wavelength for tensile strained GeSn waveguide modulators with different Sn content, which is calculated by ref. [26]. During simulation, the intensity of electric field varies from 0 to 10 MV/m at a step of 2 MV/m. Although Sn composition is different, the cut-off wavelength of all materials redshifts to MIR spectra range with the increase in the magnitude of electric

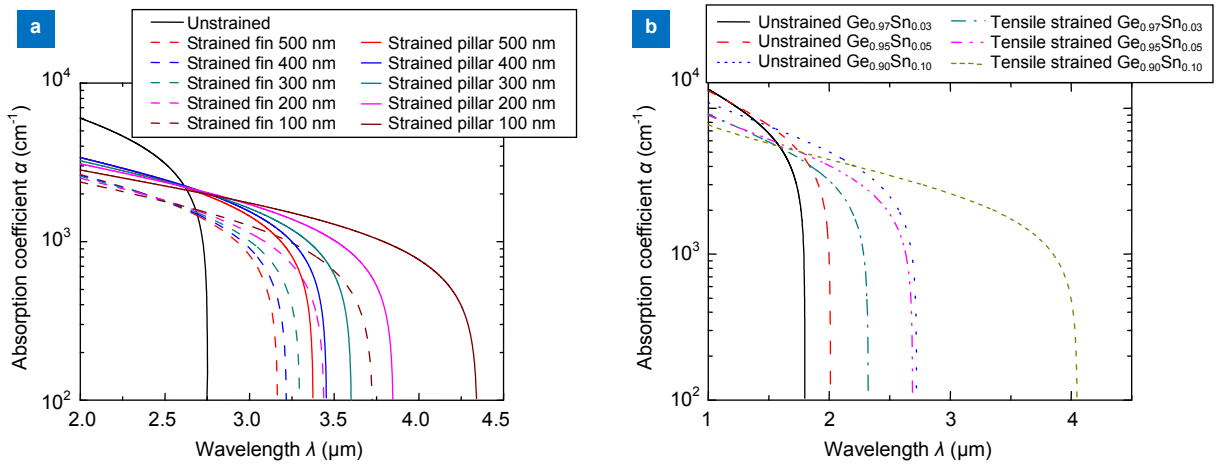

Fig. 3 | (**a**) Comparisons of the absorption spectra of relaxed and strained GeSn in fin and pillar array detectors at the Sn content of 0.1. L_{pillar} and T_{fin} feature size varys from 100 nm to 500 nm in a step of 100 nm. (**b**) Calculated absorption spectra for relaxed and tensile strained GeSn waveguide photodetectors at different Sn content. Figure reproduced from: (**a**) ref. [33], IEEE; (**b**) ref. [26], Optical Society of America.

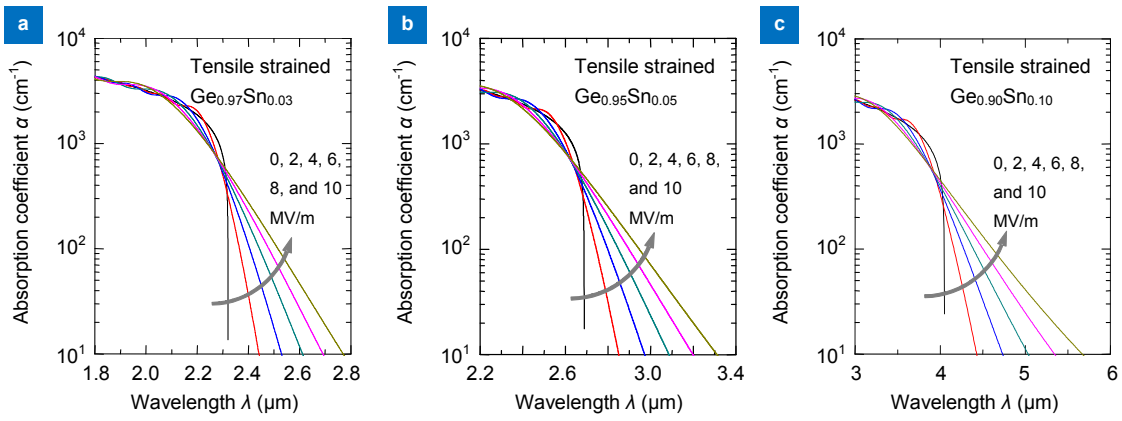

Fig. 4 | Modeled *α* as a function of wavelength at different electric fields at (a) $Ge_{0.97}Sn_{0.03}$, (b) $Ge_{0.95}Sn_{0.05}$, and (c) $Ge_{0.9}Sn_{0.1}$, respectively. Figure reproduced from ref. [26], Optical Society of America.

filed. Furthermore, it is found that the cut-off wavelength increases along with Sn content. To explore the optical transmission properties, here we employ the 2D finite-different time-domain (FDTD) method to model the $Ge_{0.90}Sn_{0.10}$ waveguide modulator. Mode profiles of transverse electric (TE) and transverse magnetic (TM) modes in the tensile strained $Ge_{0.90}Sn_{0.10}$ waveguide modulator are plotted at different wavelengths in Fig. 5. The refractive indexes for $Ge_{0.90}Sn_{0.10}$, Si_3N_4 and SiO_2 are all extracted from ref. [35]. Remarkably, single mode transmission can be observed in the waveguide for all the cases. Importantly, there is a leakage of light from waveguide with the increase in wavelength. In order to gain a deeper understanding on the optical transmission characteristics, the propagation loss versus wavelength is calculated for the tensile strained $Ge_{0.90}Sn_{0.10}$ waveguide under different electric fields in Fig. 6. For both TE and TM modes, it shows a strong dependence of propagation loss on wavelength. The propagation loss increases along with the wavelength since the optical field becomes weakly confined in the waveguide, which corresponds to the mode profiles in Fig. 5. Moreover, for a fixed wavelength, the propagation loss increases with the increase of applied electric field due to the FK effect, which results in an enhancement in the modulation depth of GeSn waveguide electro-absorption modulator.

Lasers

Accessibility of the direct bandgap material makes GeSn a decent alternative to Si in the functional photonic platform, which helps to realize a monolithically integrated laser. A GeSn/SiGeSn multiple quantum well (MQW) laser wrapped in Si_3N_4 liner stressor is proposed and investigated, as described in Fig. 7. The laser performances are thoroughly analyzed by Sn composition, injected carrier density $n_{injected}$, and quantum well number n_{well}. It is

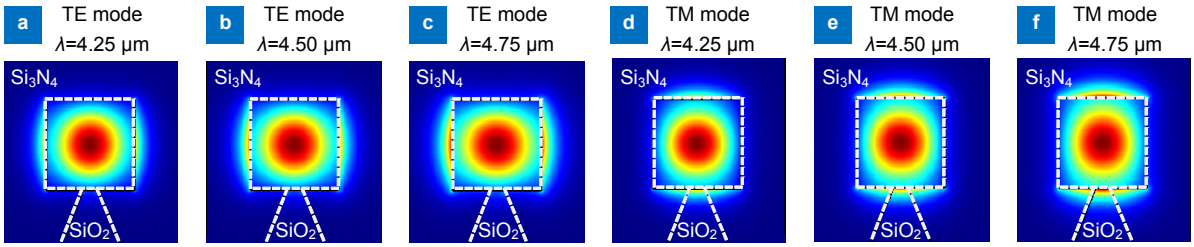

Fig. 5 | Mode profiles of both TE and TM modes at different wavelengths in $Ge_{0.90}Sn_{0.10}$ waveguide. Figure reproduced from ref. [26], Optical Society of America.

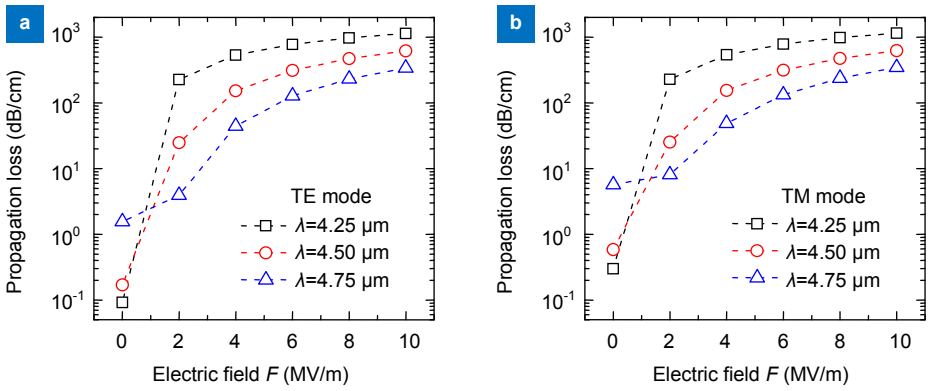

Fig. 6 | Propagation loss of (a) TE mode and (b) TM mode in tensile strained $Ge_{0.90}Sn_{0.10}$ waveguide at various biases. Figure reproduced from ref. [26], Optical Society of America.

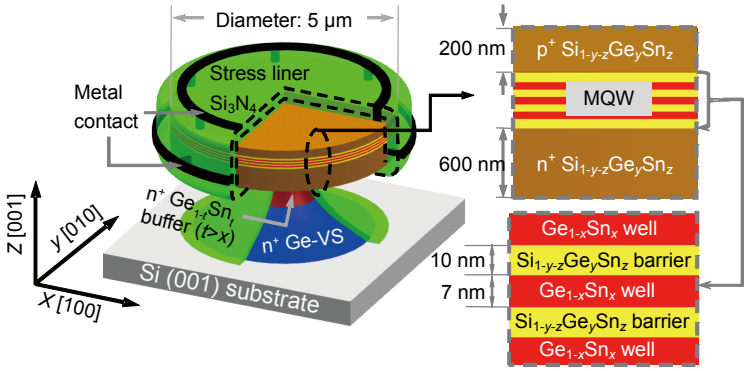

Fig. 7 | 3D schematic of the $Ge_{1-x}Sn_x/Si_{1-y-z}Ge_ySn_z$ MQW laser wrapped in a Si_3N_4 liner stressor. Figure reproduced from ref. [36], IEEE.

demonstrated that the threshold current density J_{th} reduces from 476 to 168 A/cm^2 and the optical gain is improved obviously, by introducing the Si_3N_4 liner stressor.

To analyze the impact of the Si_3N_4 liner stressor on the GeSn/SiGeSn MQW laser, strain distributions on the normal and radial cross section planes are plotted in Fig. 8. The strain along [100], [010], and [001] directions in the normal cross section plane are denoted by $\varepsilon_{[100]}$, $\varepsilon_{[010]}$, and $\varepsilon_{[001]}$, respectively. The strain contour plots indicate that [100] and [010] directions are under a tensile strain while $\varepsilon_{[001]}$ is compressive. At the center of the GeSn layer of GeSn/SiGeSn MQW laser, it can be seen that the values of $\varepsilon_{[100]}$, $\varepsilon_{[010]}$, and $\varepsilon_{[001]}$ are 0.85%, 0.85%, and -0.77%, respectively.

As shown in Fig. 9(a) and 9(b), the threshold current density J_{th} and optical gain α in GeSn/SiGeSn lasers are modeled as a function of Sn composition in GeSn wells and injected current density, respectively. Here, L_z is the thickness of the potential well. By introducing the tensile strain, there is an obvious attenuation in the J_{th} in $Ge_{0.90}Sn_{0.10}/Si_{0.161}Ge_{0.695}Sn_{0.144}$ MQW laser. It can be clearly seen that the J_{th} decreases from 476 to 168 A/cm^2 at a Sn content of 0.1. For comparison, the values of $\Gamma_{MQW,TE}\cdot g_{\Gamma\text{-}HH}$ and $\Gamma_{MQW,TM}\cdot g_{\Gamma\text{-}LH}$ are calculated as a function of injected current density J for the relaxed and tensile strained $Ge_{0.90}Sn_{0.10}/Si_{0.161}Ge_{0.695}Sn_{0.144}$ MQW lasers, as shown in Fig. 9(b). The calculation results indicate that J decreases significantly to achieve a same α for the strained $Ge_{0.90}Sn_{0.10}$ device. It should also be noted that compared to the $Ge_{0.90}Sn_{0.10}/Si_{0.161}Ge_{0.695}Sn_{0.144}$ laser, $Ge_{0.96}Sn_{0.04}/Si_{0.274}Ge_{0.611}Sn_{0.115}$ device performs an improved J under the same tensile strain, indicating the influence of the Sn component.

To better understand the impact of the gain medium on photoluminescence inside the cavity, a brief introduction is presented from the energy band structure. The subband energy difference between E_Γ and E_L is defined as ΔE. Here, E_Γ and E_L are the energies of the ground sub-band levels of Γ and L valleys, respectively. Large density of the states concentrates in L-bandedge due to the fact that the effective mass is large. It is recognized that injected carriers occupy firstly lower energy states. Consequently, there is a larger carrier leakage for large ΔE and a small value of ΔE of the material is preferable to increase the gain. Energy band structure and carrier distribution in GeSn/SiGeSn MQW are discussed in detail in ref. [36]. According to the discussion above, under tensile strain, the band structure is changed. During the injec-

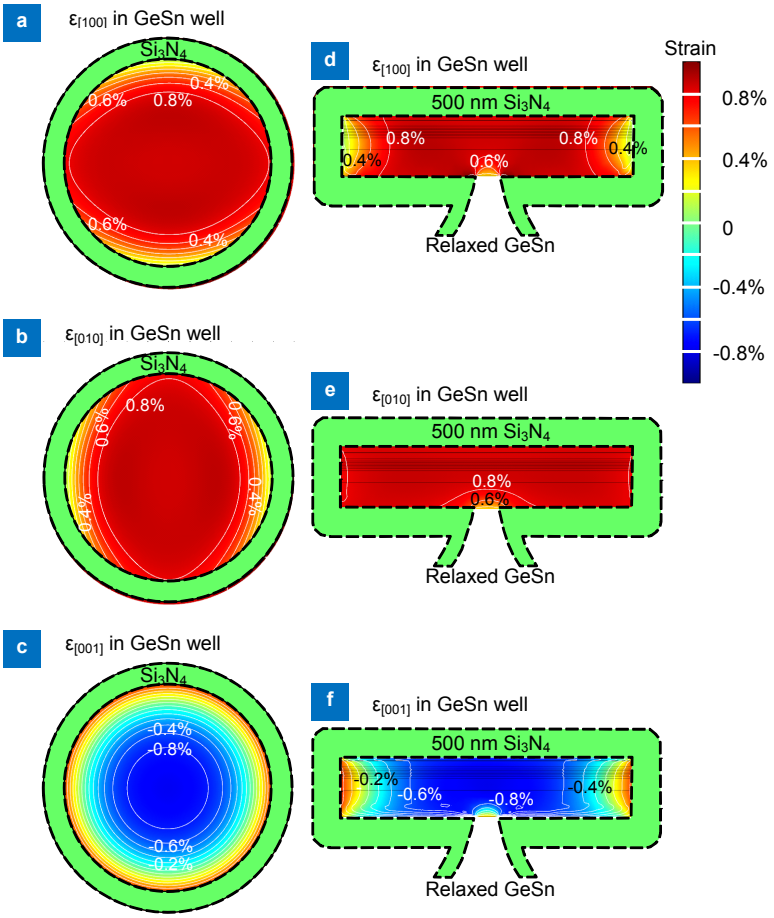

Fig. 8 | Contour plots for (a) $\varepsilon_{[100]}$, (b) $\varepsilon_{[010]}$, and (c) $\varepsilon_{[001]}$ in the normal cross section plane and (d) $\varepsilon_{[100]}$, (e) $\varepsilon_{[010]}$, and (f) $\varepsilon_{[001]}$ in the radial cross section plane in GeSn well for the $Ge_{0.90}Sn_{0.10}/Si_{0.161}Ge_{0.695}Sn_{0.144}$ MQW laser wrapped in a 500 nm Si_3N_4 liner stressor. Figure reproduced from ref. [36], IEEE.

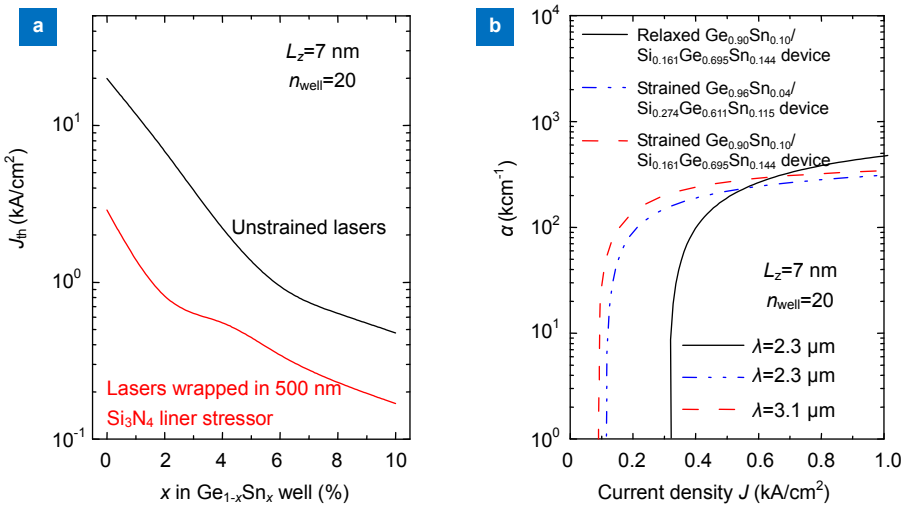

Fig. 9 | (**a**) Modeled J_{th} as a function of the Sn composition in GeSn wells for relaxed and tensile strained GeSn/SiGeSn MQW lasers wrapped in a 500 nm Si_3N_4 liner stressor. L_z is 7 nm and n_{well} is 20. (**b**) Modeled optical gain α as a function of injected current density J for the relaxed and tensile strained MQW lasers. Figure reproduced from ref. [36], IEEE.

tion of carriers, the population inversion between the sub-bandgap $E_{sub\text{-}G}$ in GeSn wells occurs for the increase of electron occupation probability in Γ conduction valley, which contributes to the improvement of light emission performance in lasers. It is believed that the Sn compositions at well layers and the strain should be carefully designed to achieve a large optical gain.

Light-emitting diode

In consideration of few experimental studies on the tensile strained GeSn light emitters up to date, we theoretically design and analyze a GeSn/SiGeSn double heterostructure (DH) light emitting diode (LED) with a microdisk structure wrapped in Si_3N_4. The impacts of Sn content on strain distributions and energy band structure are thoroughly analyzed. Moreover, the analysis of simulation results shows that the spontaneous emission rate r_{sp} and the internal quantum efficiency η_{IQE} can be improved by increasing Sn composition, carrier injection density $n_{injected}$, and n-type doping concentration n_{doping} in the GeSn active layer. The 3D schematic of a GeSn/SiGeSn DH LED with a microdisk device architecture is shown in Fig. 10.

The values of $\varepsilon_{[100]}$, $\varepsilon_{[010]}$, and $\varepsilon_{[001]}$, and volume strains in the central region for intrinsic GeSn layers are determined by the finite element method (FEM), which are extracted and compared in Fig. 11(a). One can see that there is no more change in the strain distribution. Figure 11(b) gives the $E_{G,\Gamma}$ and $E_{G,L}$ of the relaxed and strained GeSn with different Sn compositions. It can be observed that under the tensile strain, the energy of the Γ conduction valley and L conduction valley declines with the increase in Sn content. It should also be noted that the energy of the Γ conduction valley decreases more significantly than that of the L conduction valley, which leads to a decline of Sn content required for achieving the direct bandgap.

Since the light-emitting performance of the devices is dependent on r_{sp} and η_{IQE}, we first focus on r_{sp}. Detailed calculation of r_{sp} per unit volume in the energy and η_{IQE} can be seen in the ref. [37]. As depicted in Fig. 12, the total spontaneous emission spectra of the proposed device are plotted under different conditions. Considering that there are two valence bands (e.g. a light hole (LH) band and a

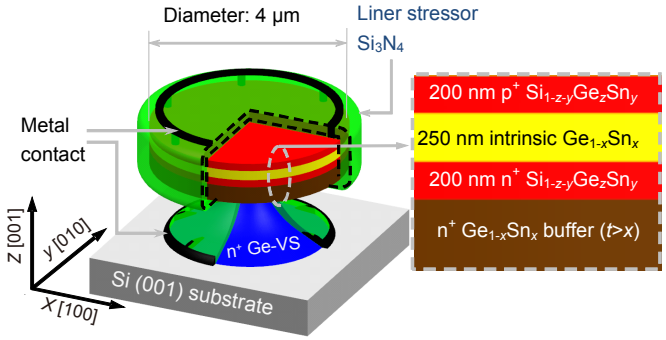

Fig. 10 | 3D schematic of lattice-matched GeSn/SiGeSn DH LED wrapped in a Si_3N_4 liner stressor. Figure reproduced from ref. [37], Optical Society of America.

heavy hole (HH) band), $r_{sp,LH}$ and $r_{sp,HH}$ are calculated, respectively, corresponding to two peaks in the spontaneous emission spectrum. Compared to the relaxed one, r_{sp} can be improved markedly in the strained device. Figure 12(b) compares the total spontaneous emission spectra with different Sn compositions. It can be clearly seen that with the same $n_{injected}$, the spontaneous emission spectra of the strained GeSn increase with the Sn content. With the same doping condition, a rapid increase in the intensity can be observed in Fig. 12(c), suggesting the similar impact of Sn content and $n_{injected}$ on the strength of spontaneous emission rate. Besides, it is worth noting that the increases of Sn composition and $n_{injected}$ bring about an opposite shift of peak position. That is, the red-

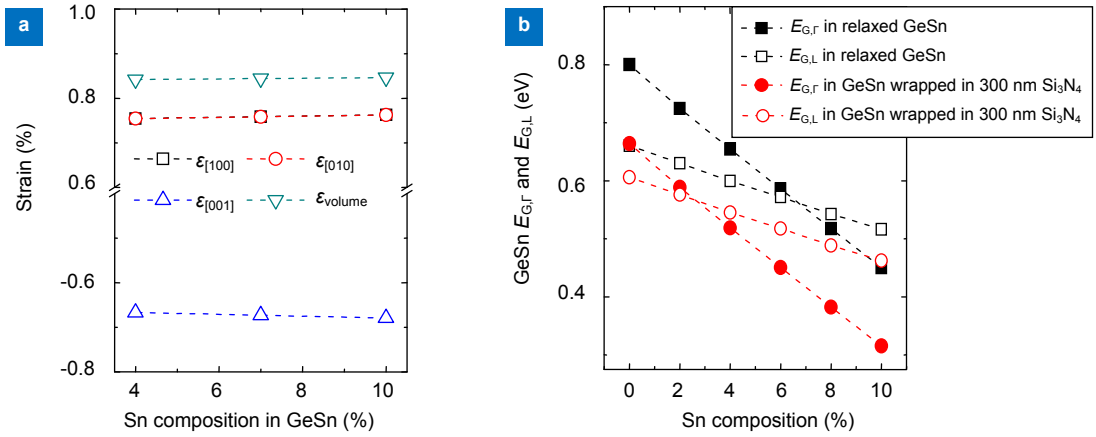

Fig. 11 | (**a**) Modeled strain components as a function of Sn composition in the intrinsic GeSn layer. (**b**) Comparison of $E_{G,\Gamma}$ and $E_{G,L}$ in relaxed and strained GeSn with various Sn compositions. Figure reproduced from ref. [37], Optical Society of America.

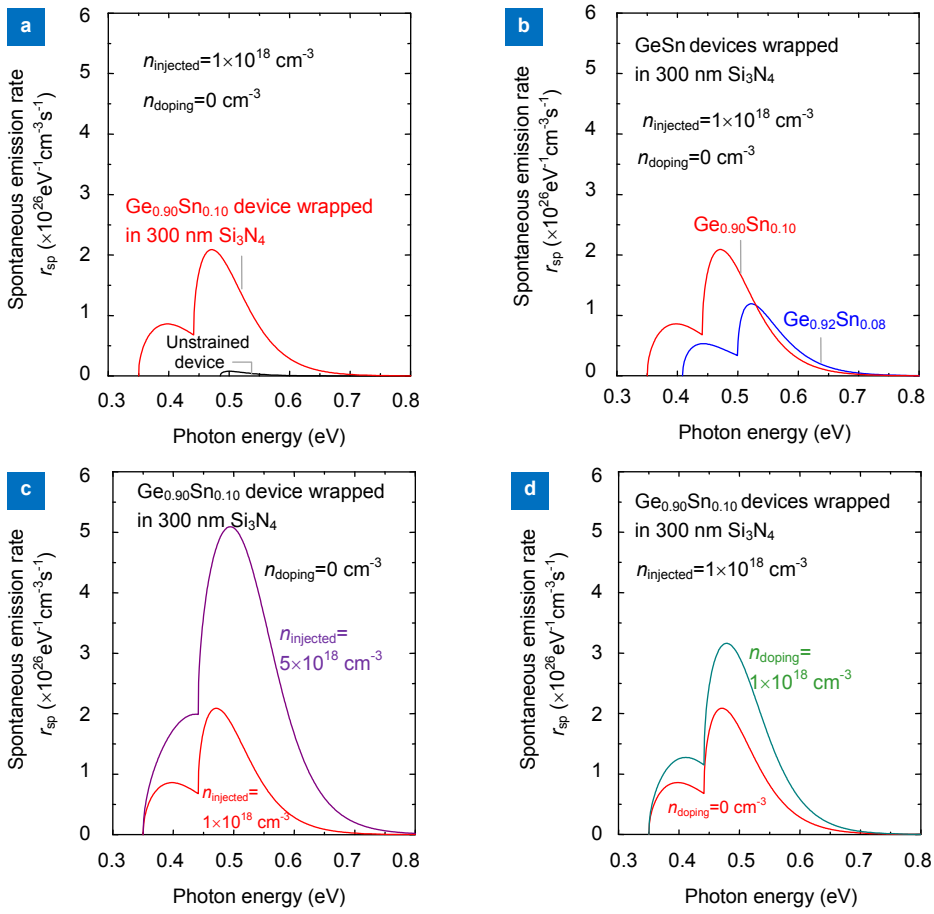

Fig. 12 | Calculated spontaneous emission spectra for the direct transition of GeSn in the lattice-matched GeSn/SiGeSn DHLEDs (**a**) **under different strain status**, (**b**) **with different Sn compositions**, (**c**) **with different $n_{injected}$, and** (**d**) **with various n_{doping}. For all the curves, the stronger and weaker peaks represent $r_{sp,HH}$ and $r_{sp,LH}$, respectively**. Figure reproduced from ref. [37], Optical Society of America.

shift is caused by increasing Sn composition while the blueshift results from improved $n_{injected}$. Figure 12(d) describes the impact of n_{doping} on r_{sp}, which shows that r_{sp} can exhibit an enhancement with the increase in the n-type doping concentration n_{doping}.

As another key factor to evaluate the light-emitting performance of the devices, the η_{IQE} is calculated as a function of Sn composition in Fig. 13. The defect-limited carrier lifetime is denoted by τ_{SRH}, which can be increased by improving the material quality of GeSn. It seems that η_{IQE} can be improved along with Sn content in GeSn layer and the devices with a large τ_{SRH} achieve an enhancement in η_{IQE} compared to those with a small τ_{SRH}. It can be seen from Fig. 13(a) that η_{IQE} of DH LEDs is enhanced significantly after introducing tensile strain for the increase of $n_{e,\Gamma}/n_{e,total}$ in the tensile strained GeSn. Here, the total electron concentration $n_{e,total}$ is the sum of those in Γ and L valleys ($n_{e,\Gamma}+n_{e,L}$). The impacts of $n_{injected}$ and n_{doping} on η_{IQE} are investigated and shown in Fig. 13(b) and 13(c). It seems that η_{IQE} shows similar $n_{injected}$-depengence and n_{doping}-dependence like r_{sp}. That is, the increase of $n_{injected}$ and n_{doping} can also improve η_{IQE} of the devices.

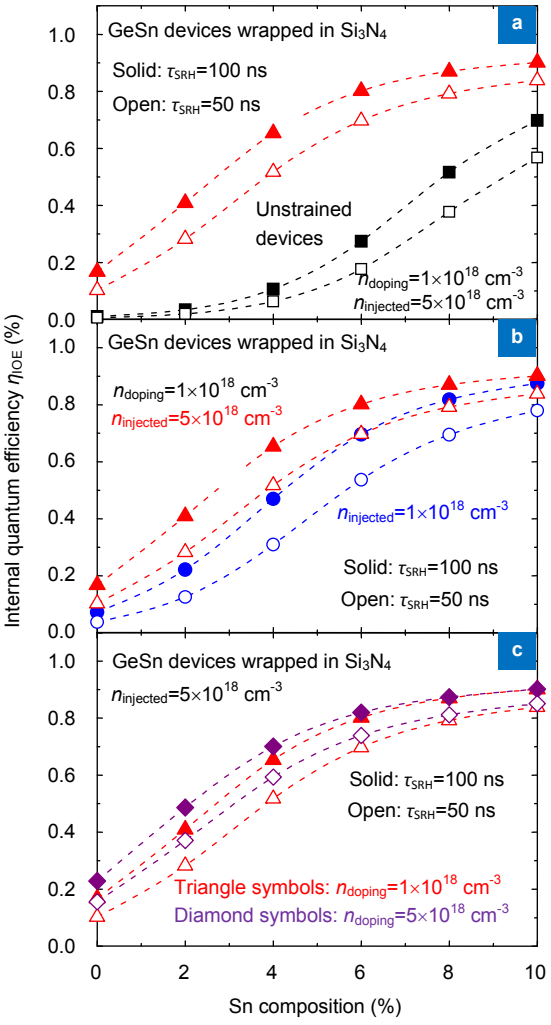

Fig. 13 | η_{IQE} versus Sn composition characteristics of lattice-matched GeSn/SiGeSn DH LEDs with the τ_{SRH} of 100 and 50 ns. (**a**) Relaxed and tensile strained GeSn devices. (**b**) Strained GeSn devices wrapped in a Si_3N_4 liner stressor with different values of $n_{injected}$. (**c**) Strained devices with different n_{doping}. Figure reproduced from ref. [37], Optical Society of America.

Outlook and summary

In the last part of this section, we will briefly discuss the possible future avenues in GeSn material. Considering that band gap can be adjusted by adding Sn content, GeSn material can be applied for light emitting devices, including laser and LED. It has been reported that the related work is underway in laser[38-40] and light emission[41-43]. However, most of work is just focused on optical pumping at low temperature and the luminous efficiency is low. GeSn material with direct bandgap leads to a small band gap (i.e., ~0.56 eV), which limits its applications in optical communication[44]. Besides, the existence of solid solubility and limitation of strain engineering also influence the performance of GeSn based devices. Above all, the photodetector with GeSn is potential for the feasibility of practical applications. It is demonstrated that there are already some achievements in photodetection[45-46]. Due to the tremendous research attention to this material, the growth of GeSn film is correspondingly explored to improve the stability and quality of GeSn film for the development of GeSn-based photonic applications[47-49]. Owing to the fast growing rate of the research on this material, the author is confident that more breakthroughs in practical applications will be achieved.

Conclusion

In summary, we discuss the recent achievements in the applications of GeSn based devices wrapped by the Si_3N_4 liner stressor. Their strain distribution is analyzed in detail by numerical simulation tools, which is introduced by the Si_3N_4 liner stressor. The calculations show that the performance can be improved by optimizing the geometric parameters. Importantly, the operating wavelength can be extended to the whole mid-infrared (2~5 μm) region, which paves the way for the monolithic and CMOS-compatible mid-infrared integrated optics applications like image sensors and optical receivers.

References

1. Mathews J, Beeler R T, Tolle J, Xu C, Roucka R *et al*. Direct-gap photoluminescence with tunable emission wavelength in $Ge_{1-y}Sn_y$ alloys on silicon. *Appl Phys Lett* **97**, 221912 (2010).
2. Chen R, Lin H, Huo Y J, Hitzman C, Kamins T I *et al*. Increased photoluminescence of strain-reduced, high-Sn composition $Ge_{1-x}Sn_x$ alloys grown by molecular beam epitaxy. *Appl Phys Lett* **99**, 181125 (2011).
3. Lin H, Chen R, Lu W S, Huo Y J, Kamins T I *et al*. Investigation of the direct band gaps in $Ge_{1-x}Sn_x$ alloys with strain control by photoreflectance spectroscopy. *Appl Phys Lett* **100**, 102109 (2012).
4. Yin W J, Gong X G, Wei S H. Origin of the unusually large

band-gap bowing and the breakdown of the band-edge distribution rule in the Sn_xGe_{1-x} alloys. *Phys Rev B* **78**, 161203 (2008).
5. de Guevara H P L, Rodríguez A G, Navarro-Contreras H, Vidal M A. Structural and optical properties of $Ge_{1-x}Sn_x$ alloys grown on GaAs (001) by R. F. Magnetron Sputtering. *ECS Trans* **64**, 393−400 (2004).
6. D'Costa V R, Cook C S, Birdwell A G, Littler C L, Canonico M *et al*. Optical critical points of thin-film $Ge_{1-y}Sn_y$ alloys: A comparative $Ge_{1-y}Sn_y/Ge_{1-x}Si_x$ study. *Phys Rev B* **73**, 125207 (2006).
7. Soref R A, Perry C H. Predicted band gap of the new semiconductor SiGeSn. *J Appl Phys* **69**, 539−541 (1991).
8. He G, Atwater H A. Interband transitions in Sn_xGe_{1-x} alloys. *Phys Rev Lett* **79**, 1937−1940 (1997).
9. Moontragoon P, Ikonić Z, Harrison P. Band structure calculations of Si-Ge-Sn alloys: achieving direct band gap materials. *Semicond Sci Technol* **22**, 742−748 (2007).
10. Eckhardt C, Hummer K, Kresse G. Indirect-to-direct gap transition in strained and unstrained Sn_xGe_{1-x} alloys. *Phys Rev B* **89**, 165201 (2014).
11. Attiaoui A, Moutanabbir O. Indirect-to-direct band gap transition in relaxed and strained $Ge_{1-x-y}Si_xSn_y$ ternary alloys. *J Appl Phys* **116**, 063712 (2014).
12. Wirths S, Ikonic Z, Tiedemann A T, Holländer B, Stoica T *et al*. Tensely strained GeSn alloys as optical gain media. *Appl Phys Lett* **103**, 192110 (2013).
13. Wirths S, Geiger R, von den Driesh N, Mussler G, Stoica T *et al*. Lasing in direct-bandgap GeSn alloy grown on Si. *Nat Photonics* **9**, 88−92 (2015).
14. Soref R, Kouvetakis J, Tolle J, Menendez J, D'Costa V. Advances in SiGeSn technology. *J Mater Res* **22**, 3281−3291 (2007).
15. Bauer M R, Taraci J, Tolle J, Chizmeshya A V G, Zollner S *et al*. Ge–Sn semiconductors for band-gap and lattice engineering. *Appl Phys Lett* **81**, 2992−2994 (2002).
16. Kouvetakis J, Chizmeshya A V G. New classes of Si-based photonic materials and device architectures via designer molecular routes. *J Mater Chem* **17**, 1649–1655 (2007).
17. Sun G, Soref R A, Cheng H H. Design of a Si-based lattice-matched room-temperature GeSn/GeSiSn multi-quantum-well mid-infrared laser diode. *Opt Express* **18**, 19957–19965 (2010).
18. Gassenq A, Gencarelli F, Van Campenhout J, Shimura Y, Loo R *et al*. GeSn/Ge heterostructure short-wave infrared photodetectors on silicon. *Opt Express* **20**, 27297–27303 (2012).
19. Oehme M, Schmid M, Kaschel M, Gollhofer M, Widmann D *et al*. GeSn p-i-n detectors integrated on Si with up to 4% Sn. *Appl Phys Lett* **101**, 141110 (2012).
20. Oehme M, Kostecki K, Schmid M, Oliveira F, Kasper E *et al*. Epitaxial growth of strained and unstrained GeSn alloys up to 25% Sn. *Thin Solid Films* **557**, 169–172 (2014).
21. Taoka N, Capellini G, von den Driesch N, Buca D, Zaumseil P *et al*. Sn migration control at high temperature due to high deposition speed for forming high-quality GeSn layer. *Appl Phys Express* **9**, 031201 (2016).
22. Li H, Chang C, Chen T P, Cheng H H, Shi Z W *et al*. Characteristics of Sn segregation in Ge/GeSn heterostructures. *Appl Phys Lett* **105**, 151906 (2014).
23. Wang W, Li L Z, Zhou Q, Pan J S, Zhang Z *et al*. Tin surface segregation, desorption, and island formation during post-growth annealing of strained epitaxial $Ge_{1-x}Sn_x$ layer on Ge (001) substrate. *Appl Surf Sci* **321**, 240–244 (2014).
24. Wang W, Dong Y, Zhou Q, Tok E S, Yeo Y C. Germanium-tin interdiffusion in strained Ge/GeSn multiple-quantum-well structure. *J Phys D Appl Phys* **49**, 225102 (2016).
25. Gupta S, Magyari-Köpe B, Nishi Y, Saraswat K C. Achieving direct band gap in germanium through integration of Sn alloying and external strain. *J Appl Phys* **113**, 073707 (2013).
26. Zhang Q F, Liu Y, Yan J, Zhang C F, Hao Y *et al*. Theoretical investigation of tensile strained GeSn waveguide with Si_3N_4 liner stressor for mid-infrared detector and modulator applications. *Opt Express* **23**, 7924–7932 (2015).
27. Fujisawa T, Saitoh K. Material gain analysis of GeSn/SiGeSn quantum wells for mid-infrared Si-based light sources based on many-body theory. *IEEE J Quantum Electron* **51**, 7100108 (2015).
28. Zhu Y H, Xu Q, Fan W J, Wang J W. Theoretical gain of strained $GeSn_{0.02}/Ge_{1-x-y'}$ $Si_xSn_{y'}$ quantum well laser. *J Appl Phys* **107**, 073108 (2010).
29. Zhang Q F, Liu Y, Yan J, Zhang C F, Hao Y *et al*. Simulation investigation of tensile strained GeSn fin photodetector with Si_3N_4 liner stressor for extension of absorption wavelength. *Opt Express* **23**, 739–746 (2015).
30. Capellini G, Reich C, Guha S, Yamamoto Y, Lisker M *et al*. Tensile Ge microstructures for lasing fabricated by means of a silicon complementary metal-oxide-semiconductor process. *Opt Express* **22**, 399–410 (2014).
31. Fenrich C S, Chen X C, Chen R, Huang Y C, Chung H *et al*. Strained pseudomorphic $Ge_{1-x}Sn_x$ multiple quantum well microdisk using SiN_y stressor layer. *ACS Photonics* **3**, 2231–2236 (2016).
32. El Kurdi M, Prost M, Ghrib A, Sauvage S, Checoury X *et al*. Direct band gap germanium microdisks obtained with silicon nitride stressor layers. *ACS Photonics* **3**, 443–448 (2016).
33. Zhang Q F, Liu Y, Zhang C F, Huang Q Z, Hao Y *et al*. Tensile-strained mid-infrared GeSn detectors wrapped in Si_3N_4 liner stressor: theoretical investigation of impact of device architectures. *IEEE Photonics J* **7**, 6803208 (2015).
34. Basu P K. *Theory of Optical Processes in Semiconductors: Bulk and Microstructures* (Oxford, UK: Clarendon, 1997).
35. Palik E D. *Handbook of Optical Constants of Solids* (San Diego: Academic, 1998).
36. Liu Y, Fang C Z, Gao X, Han G Q, Zhang Q F *et al*. Theoretical investigation of tensile-strained GeSn/SiGeSn multiple quantum well laser wrapped in Si_3N_4 liner stressor. *IEEE Photonics J* **10**, 1500609 (2018).
37. Zhang Q F, Liu Y, Han G Q, Shao Y, Gao X *et al*. Theoretical analysis of performance enhancement in GeSn/SiGeSn light-emitting diode enabled by Si_3N_4 liner stressor technique. *Appl Opt* **55**, 9668–9674 (2016).
38. Al-Kabi S, Ghetmiri S A, Margetis J, Pham T, Zhou Y Y *et al*. Optically pumped Si-based edge-emitting GeSn laser. In *Proceedings of Conference on Lasers and Electro-Optics* SW4C.1 (OSA, 2017); http://doi.org/10.1364/CLEO_SI.2017.SW4C.1.
39. Stange D, von den Driesch N, Zabel T, Armand-Pilon F, Marzban B *et al*. Reduced threshold microdisk lasers from GeSn/SiGeSn heterostructures. In *Proceedings of the 14th International Conference on Group IV Photonics* 15–16 (IEEE, 2017); http://doi.org/10.1109/GROUP4.2017.8082173.
40. Margetis J, Al-Kabi S, Du W, Dou W, Zhou Y Y *et al*. Si-based GeSn lasers with wavelength coverage of 2–3 μm and operating temperatures up to 180 K. *ACS Photonics* **5**, 827–833 (2018).
41. Millar R W, Dumas D C S, Gallacher K F, Jahandar P, MacGregor C *et al*. Mid-infrared light emission >3 μm wavelength from tensile strained GeSn microdisks. *Opt Express* **25**,

25374–25385 (2017).
42. Stange D, von den Driesch N, Rainko D, Roesgaard S, Povstugar I *et al*. Short-wave infrared LEDs from GeSn/SiGeSn multiple quantum wells. *Optica* **4**, 185–188 (2017).
43. Millar R W, Dumas D C S, Gallacher K, Jahandar P, Myronov M *et al*. Tensile strained GeSn mid-infrared light emitters. In Proceedings of the *14th International Conference on Group IV Photonics* 49–50 (IEEE, 2017); http://doi.org/10.1109/GROUP4.2017.8082190.
44. Ghetmiri S A, Du W, Margetis J, Mosleh A, Cousar L *et al*. Direct-bandgap GeSn grown on silicon with 2230 nm photoluminescence. *Appl Phys Lett* **105**, 151109 (2014).
45. Tsai C H, Chang G E. GeSn/Ge quantum well photodetectors for short-wave infrared photodetection: experiments and modeling. *Proc SPIE* **10231**, 102310J (2017).
46. Huang B J, Lin J H, Cheng H H, Chang G E. GeSn resonant-cavity-enhanced photodetectors on silicon-on-insulator platforms. *Opt Lett* **43**, 1215–1218 (2018).
47. Grant P C, Dou W, Alharthi B, Grant J M, Mosleh A *et al*. Comparison study of the low temperature growth of dilute GeSn and Ge. *Jf Vac Sci Technol B Nanotechnol Microelectron Mater Process Meas Phenom* **35**, 061204 (2017).
48. Chen N L, Lin G Y, Zhang L, Li C, Chen S Y *et al*. Low-temperature formation of GeSn nanocrystallite thin films by sputtering Ge on self-assembled Sn nanodots on SiO_2/Si substrate. *Jpn J Appl Phys* **56**, 050301 (2017).
49. Khiangte K R, Rathore J S, Schmidt J, Osten H J, Laha A *et al*. Wafer-scale all-epitaxial GeSn-on-insulator on Si(111) by molecular beam epitaxy. https://arxiv.org/pdf/1802.03150.

Acknowledgements

The authors thank National Natural Science Foundation of China (Grant No. 61534004, 61604112 and 61622405).

Competing interests

The authors declare no competing financial interests.